Heavy quark tagging with leptons in the ALEPH detector

D. Buskulic, D. Casper, I. de Bonis, D. Decamp, P. Ghez, C. Goy, J P. Lees, M N. Minard, P. Odier, B. Pietrzyk, et al.

EUROPEAN ORGANIZATION FOR NUCLEAR RESEARCH

CERN-PPE/94-023
27 Jan 1994

Heavy Quark Tagging with Leptons in the ALEPH Detector.

The ALEPH Collaboration

Abstract

Semileptonic decays of heavy quarks yield prompt leptons which can be used to identify events resulting from the decays of the Z into $c\bar{c}$ and $b\bar{b}$ pairs. The procedures adopted to obtain clean samples of inclusive leptons with the ALEPH detector are described. Electron identification makes use of ionization measurements in the tracking system of ALEPH and the shape of showers in the electromagnetic calorimeter. Muons are identified using the tracking capabilities of the Hadron Calorimeter, together with the Muon Chamber information. Distinguishing the sources of prompt lepton production requires the determination of the lepton's transverse momentum with respect to the parent hadron's flight direction. As the latter is not directly measurable, the results of an algorithm are presented which uses the information produced by the ALEPH detector to achieve the most effective axis from which the transverse momentum should be measured.

Submitted to N.I.M.

The ALEPH Collaboration

D. Buskulic, D. Casper, I. De Bonis, D. Decamp, P. Ghez, C. Goy, J.-P. Lees, M.-N. Minard, P. Odier, B. Pietrzyk

Laboratoire de Physique des Particules (LAPP), IN^{2}P^3-CNRS, 74019 Annecy-le-Vieux Cedex, France

F. Ariztizabal, P. Comas, J.M. Crespo, I. Efthymiopoulos, E. Fernandez, M. Fernandez-Bosman, V. Gaitan, Ll. Garrido,[29] M. Martinez, T. Mattison,[30] S. Orteu, A. Pacheco, C. Padilla, A. Pascual

Institut de Fisica d'Altes Energies, Universitat Autonoma de Barcelona, 08193 Bellaterra (Barcelona), Spain[7]

D. Creanza, M. de Palma, A. Farilla, G. Iaselli, G. Maggi, N. Marinelli, S. Natali, S. Nuzzo, A. Ranieri, G. Raso, F. Romano, F. Ruggieri, G. Selvaggi, L. Silvestris, P. Tempesta, G. Zito

Dipartimento di Fisica, INFN Sezione di Bari, 70126 Bari, Italy

Y. Chai, D. Huang, X. Huang, J. Lin, T. Wang, Y. Xie, D. Xu, R. Xu, J. Zhang, L. Zhang, W. Zhao

Institute of High-Energy Physics, Academia Sinica, Beijing, The People's Republic of China[8]

G. Bonvicini, J. Boudreau,[25] H. Drevermann, R.W. Forty, G. Ganis, C. Gay,[3] M. Girone, R. Hagelberg, J. Harvey, J. Hilgart,[27] R. Jacobsen, B. Jost, J. Knobloch, I. Lehraus, M. Maggi, C. Markou, P. Mato, H. Meinhard, A. Minten, R. Miquel, P. Palazzi, J.R. Pater, J.A. Perlas, P. Perrodo, J.-F. Pusztaszeri, F. Ranjard, L. Rolandi, J. Rothberg,[2] T. Ruan, M. Saich, D. Schlatter, M. Schmelling, F. Sefkow,[6] W. Tejessy, I.R. Tomalin, R. Veenhof, H. Wachsmuth, S. Wasserbaech,[2] W. Wiedenmann, T. Wildish, W. Witzeling, J. Wotschack

European Laboratory for Particle Physics (CERN), 1211 Geneva 23, Switzerland

Z. Ajaltouni, M. Bardadin-Otwinowska, A. Barres, C. Boyer, A. Falvard, P. Gay, C. Guicheney, P. Henrard, J. Jousset, B. Michel, J-C. Montret, D. Pallin, P. Perret, F. Podlyski, J. Proriol, F. Saadi

Laboratoire de Physique Corpusculaire, Université Blaise Pascal, IN^{2}P^3-CNRS, Clermont-Ferrand, 63177 Aubière, France

T. Fearnley, J.B. Hansen, J.D. Hansen, J.R. Hansen, P.H. Hansen, S.D. Johnson, R. Møllerud, B.S. Nilsson[1]

Niels Bohr Institute, 2100 Copenhagen, Denmark[9]

A. Kyriakis, E. Simopoulou, I. Siotis, A. Vayaki, K. Zachariadou

Nuclear Research Center Demokritos (NRCD), Athens, Greece

J. Badier, A. Blondel, G. Bonneaud, J.C. Brient, P. Bourdon, G. Fouque, L. Passalacqua, A. Rougé, M. Rumpf, R. Tanaka, M. Verderi, H. Videau

Laboratoire de Physique Nucléaire et des Hautes Energies, Ecole Polytechnique, IN^{2}P^3-CNRS, 91128 Palaiseau Cedex, France

D.J. Candlin, M.I. Parsons, E. Veitch

Department of Physics, University of Edinburgh, Edinburgh EH9 3JZ, United Kingdom[10]

E. Focardi, L. Moneta, G. Parrini

Dipartimento di Fisica, Università di Firenze, INFN Sezione di Firenze, 50125 Firenze, Italy

M. Corden, M. Delfino,[12] C. Georgiopoulos, D.E. Jaffe, D. Levinthal[15]

Supercomputer Computations Research Institute, Florida State University, Tallahassee, FL 32306-4052, USA [13,14]

A. Antonelli, G. Bencivenni, G. Bologna,[4] F. Bossi, P. Campana, G. Capon, F. Cerutti, V. Chiarella, G. Felici, P. Laurelli, G. Mannocchi,[5] F. Murtas, G.P. Murtas, M. Pepe-Altarelli, S. Salomone

Laboratori Nazionali dell'INFN (LNF-INFN), 00044 Frascati, Italy

P. Colrain, I. ten Have, I.G. Knowles, J.G. Lynch, W. Maitland, W.T. Morton, C. Raine, P. Reeves, J.M. Scarr, K. Smith, M.G. Smith, A.S. Thompson, S. Thorn, R.M. Turnbull

Department of Physics and Astronomy, University of Glasgow, Glasgow G12 8QQ,United Kingdom[10]

U. Becker, O. Braun, C. Geweniger, P. Hanke, V. Hepp, E.E. Kluge, A. Putzer,[1] B. Rensch, M. Schmidt H. Stenzel, K. Tittel, M. Wunsch

Institut für Hochenergiephysik, Universität Heidelberg, 69120 Heidelberg, Fed. Rep. of Germany[16]

R. Beuselinck, D.M. Binnie, W. Cameron, M. Cattaneo, D.J. Colling, P.J. Dornan, J.F. Hassard, N. Konstantinidis, A. Moutoussi, J. Nash, D.G. Payne, G. San Martin, J.K. Sedgbeer, A.G. Wright

Department of Physics, Imperial College, London SW7 2BZ, United Kingdom[10]

P. Girtler, D. Kuhn, G. Rudolph, R. Vogl

Institut für Experimentalphysik, Universität Innsbruck, 6020 Innsbruck, Austria[18]

C.K. Bowdery, T.J. Brodbeck, A.J. Finch, F. Foster, G. Hughes, D. Jackson, N.R. Keemer, M. Nuttall, A. Patel, T. Sloan, S.W. Snow, E.P. Whelan

Department of Physics, University of Lancaster, Lancaster LA1 4YB, United Kingdom[10]

A. Galla, A.M. Greene, K. Kleinknecht, J. Raab, B. Renk, H.-G. Sander, H. Schmidt, S.M. Walther, R. Wanke, B. Wolf

Institut für Physik, Universität Mainz, 55099 Mainz, Fed. Rep. of Germany[16]

A.M. Bencheikh, C. Benchouk, A. Bonissent, D. Calvet, J. Carr, P. Coyle, C. Diaconu, F. Etienne, D. Nicod, P. Payre, L. Roos, D. Rousseau, P. Schwemling, M. Talby

Centre de Physique des Particules, Faculté des Sciences de Luminy, IN²P³-CNRS, 13288 Marseille, France

S. Adlung, R. Assmann, C. Bauer, W. Blum, D. Brown, P. Cattaneo,[23] B. Dehning, H. Dietl, F. Dydak,[21] M. Frank, A.W. Halley, K. Jakobs, J. Lauber, G. Lütjens, G. Lutz, W. Männer, H.-G. Moser, R. Richter, J. Schröder, A.S. Schwarz, R. Settles, H. Seywerd, U. Stierlin, U. Stiegler, R. St. Denis, G. Wolf

Max-Planck-Institut für Physik, Werner-Heisenberg-Institut, 80805 München, Fed. Rep. of Germany[16]

R. Alemany, J. Boucrot,[1] O. Callot, A. Cordier, M. Davier, L. Duflot, J.-F. Grivaz, Ph. Heusse, P. Janot, D.W. Kim,[19] F. Le Diberder, J. Lefrançois, A.-M. Lutz, G. Musolino, M.-H. Schune, J.-J. Veillet, I. Videau

Laboratoire de l'Accélérateur Linéaire, Université de Paris-Sud, IN²P³-CNRS, 91405 Orsay Cedex, France

D. Abbaneo, G. Bagliesi, G. Batignani, U. Bottigli, C. Bozzi, G. Calderini, M. Carpinelli, M.A. Ciocci, V. Ciulli, R. Dell'Orso, I. Ferrante, F. Fidecaro, L. Foà,[1] F. Forti, A. Giassi, M.A. Giorgi, A. Gregorio, F. Ligabue, A. Lusiani, P.S. Marrocchesi, E.B. Martin, A. Messineo, F. Palla, G. Rizzo, G. Sanguinetti, P. Spagnolo, J. Steinberger, R. Tenchini,[1] G. Tonelli,[28] G. Triggiani, A. Valassi, C. Vannini, A. Venturi, P.G. Verdini, J. Walsh

Dipartimento di Fisica dell'Università, INFN Sezione di Pisa, e Scuola Normale Superiore, 56010 Pisa, Italy

A.P. Betteridge, Y. Gao, M.G. Green, D.L. Johnson, P.V. March, T. Medcalf, Ll.M. Mir, I.S. Quazi, J.A. Strong

Department of Physics, Royal Holloway & Bedford New College, University of London, Surrey TW20 OEX, United Kingdom[10]

V. Bertin, D.R. Botterill, R.W. Clifft, T.R. Edgecock, S. Haywood, M. Edwards, P.R. Norton, J.C. Thompson

Particle Physics Dept., Rutherford Appleton Laboratory, Chilton, Didcot, Oxon OX11 OQX, United Kingdom[10]

B. Bloch-Devaux, P. Colas, H. Duarte, S. Emery, W. Kozanecki, E. Lançon, M.C. Lemaire, E. Locci, B. Marx, P. Perez, J. Rander, J.-F. Renardy, A. Rosowsky, A. Roussarie, J.-P. Schuller, J. Schwindling, D. Si Mohand, B. Vallage

Service de Physique des Particules, DAPNIA, CE-Saclay, 91191 Gif-sur-Yvette Cedex, France[17]

R.P. Johnson, A.M. Litke, G. Taylor, J. Wear

Institute for Particle Physics, University of California at Santa Cruz, Santa Cruz, CA 95064, USA[22]

W. Babbage, C.N. Booth, C. Buttar, S. Cartwright, F. Combley, I. Dawson, L.F. Thompson

Department of Physics, University of Sheffield, Sheffield S3 7RH, United Kingdom[10]

A. Böhrer, S. Brandt, G. Cowan,[1] E. Feigl, C. Grupen, G. Lutters, J. Minguet-Rodriguez, F. Rivera,[26] P. Saraiva, U. Schäfer, L. Smolik

Fachbereich Physik, Universität Siegen, 57068 Siegen, Fed. Rep. of Germany[16]

L. Bosisio, R. Della Marina, G. Giannini, B. Gobbo, L. Pitis, F. Ragusa[20]

Dipartimento di Fisica, Università di Trieste e INFN Sezione di Trieste, 34127 Trieste, Italy

L. Bellantoni, W. Chen, J.S. Conway,[24] Z. Feng, D.P.S. Ferguson, Y.S. Gao, J. Grahl, J.L. Harton, O.J. Hayes, H. Hu, J.M. Nachtman, Y.B. Pan, Y. Saadi, M. Schmitt, I. Scott, V. Sharma, J.D. Turk, A.M. Walsh, F.V. Weber, Sau Lan Wu, X. Wu, M. Zheng, J.M. Yamartino, G. Zobernig

Department of Physics, University of Wisconsin, Madison, WI 53706, USA[11]

---

[1] Now at CERN, PPE Division, 1211 Geneva 23, Switzerland.
[2] Permanent address: University of Washington, Seattle, WA 98195, USA.
[3] Now at Harvard University, Cambridge, MA 02138, U.S.A.
[4] Also Istituto di Fisica Generale, Università di Torino, Torino, Italy.
[5] Also Istituto di Cosmo-Geofisica del C.N.R., Torino, Italy.
[6] Now at DESY, Hamburg, Germany.
[7] Supported by CICYT, Spain.
[8] Supported by the National Science Foundation of China.
[9] Supported by the Danish Natural Science Research Council.
[10] Supported by the UK Science and Engineering Research Council.
[11] Supported by the US Department of Energy, contract DE-AC02-76ER00881.
[12] On leave from Universitat Autonoma de Barcelona, Barcelona, Spain.
[13] Supported by the US Department of Energy, contract DE-FG05-92ER40742.
[14] Supported by the US Department of Energy, contract DE-FC05-85ER250000.
[15] Present address: Lion Valley Vineyards, Cornelius, Oregon, U.S.A.
[16] Supported by the Bundesministerium für Forschung und Technologie, Fed. Rep. of Germany.
[17] Supported by the Direction des Sciences de la Matière, C.E.A.
[18] Supported by Fonds zur Förderung der wissenschaftlichen Forschung, Austria.
[19] Permanent address: Kangnung National University, Kangnung, Korea.
[20] Now at Dipartimento di Fisica, Università di Milano, Milano, Italy.
[21] Also at CERN, PPE Division, 1211 Geneva 23, Switzerland.
[22] Supported by the US Department of Energy, grant DE-FG03-92ER40689.
[23] Now at Università di Pavia, Pavia, Italy.
[24] Now at Rutgers University, Piscataway, NJ 08854, USA.
[25] Now at FERMILAB, Batavia, IL 60510, U.S.A.
[26] Partially supported by Colciencias, Colombia.
[27] Now at SSCL, Dallas 75237-3946, TX, U.S.A.
[28] Also at Istituto di Matematica e Fisica, Università di Sassari, Sassari, Italy.
[29] Permanent address: Dept. d'Estructura i Constituens de la Materia, Universitat de Barcelona, 08208 Barcelona, Spain.
[30] Now at SLAC, Stanford, CA 94309, U.S.A.

1 Introduction

Approximately 20% of the decays of hadrons containing a c or b quark give a direct electron or muon, and this may be used to identify (tag) $c\bar{c}$ and $b\bar{b}$ final states in Z decay from e^+e^- annihilations at LEP. Such leptons form approximately 1% of all charged particles produced and hence to achieve a satisfactory tagging performance a detector must have excellent hadron rejection as well as efficient lepton identification. True leptons also result from Dalitz decays and photon conversions to electron pairs, and from the decays of charged π or K mesons to muons. These are referred to as non–prompt leptons, even though Dalitz electrons originate near the primary interaction point.

In this paper the procedures which are adopted with the ALEPH detector for the isolation of a pure sample of prompt final state leptons in hadronic Z decays are described. In sections 2, 3 and 4, brief descriptions of the ALEPH detector, the selection of hadronic Z decays and the basic tagging procedures are given. These are followed in sections 5 and 6 with detailed descriptions of the algorithms used to identify electrons and muons and to minimize background to the prompt sample.

The various sources of prompt leptons are distinguished primarily on the basis of their momenta and transverse momenta with respect to the direction of the decaying hadron. In section 7 there is a discussion of the choice of the axis from which the transverse momentum should be defined to achieve maximum separation of the primary b decay signal. This is based on the predicted responses of the ALEPH detector to simulated events containing semileptonic primary and secondary b decays, and primary c decays. These techniques are used in several analyses, particularly those in reference [1].

2 The Aleph detector

The ALEPH detector has been described in detail elsewhere [2]. Charged tracks are deflected by a 1.5T magnetic field coaxial with the electron and positron beams and measured by three cylindrical position detectors, a two plane silicon vertex detector (VDET), with both $r-\phi$ and z readout, and 8 layer axial drift chamber (ITC) and a large time projection chamber (TPC) which provides 21 space points for fully crossing tracks. All three detectors cover 70% or more of the solid angle and yield a momentum accuracy

$$\delta P/P = 0.0006P \quad (P \; in \; GeV/c)$$

The ITC and TPC alone cover 95% of the solid angle and yield a momentum accuracy of $\delta P/P = 0.0008P$. The TPC also provides up to 330 measurements of the specific ionization, $\mathrm{d}E/\mathrm{d}x$.

Outside the TPC but inside the coil is the electromagnetic calorimeter (ECAL) which is constructed of 45 layers of lead interleaved with proportional wire chambers. It has an energy resolution

$$\delta E/E = 0.19/\sqrt{E} + 0.01 \quad (E \; in \; GeV)$$

It is used, together with the dE/dx measurements to identify electrons.

The hadron calorimeter (HCAL) is formed by the iron of the magnet return yoke interleaved with 23 layers of streamer tubes which provide a two dimensional measurement of muon tracks and a view of the hadronic shower development. It is surrounded by the muon chambers, which are double layers of streamer tubes with three dimensional digital readout at 7.5 hadronic interaction lengths from the primary interaction point. Muons are identified using the digital readout from both the muon chambers and the HCAL.

Additional details on the ALEPH detector are found in the appropriate following sections.

3 Data sample selection

Hadronic events are selected using charged track information alone. At least 5 tracks must be reconstructed by the TPC in the event, and they must satisfy the following requirements:

- the number of TPC three–dimensional points used in the fit for the track helix must be at least four. This eliminates most fake tracks and badly fitted ones.
- the track must pass through a cylinder centred around the fitted average beam position, with a radius of 2 cm and a length of 10 cm. This cut rejects badly fitted tracks or particles originating from a vertex far from the interaction point, as well as cosmic background.
- the track must make an angle greater than 18.2° with the beam axis; this ensures that at least six pad rows in the TPC are traversed.

A cut on the total visible charged energy is applied in order to remove two photon events and beam–gas interactions; the sum of energy of all the reconstructed charged tracks must be greater than 10% of the centre of mass energy. The total efficiency of this selection is 97.5% [3]. This is independent of flavour to better than 0.1%, although cuts applied later in defining the jet direction introduce a larger bias of typically 0.6%. The background contamination from two–photon events and $Z \to \tau^+\tau^-$ is less than 0.3%.

For lepton identification, tighter cuts with respect to those defining a "good track" for the hadronic selection are applied, in order reduce backgrounds from hadron decays in flight ($\pi, K \to \mu^{\pm}$) and photon conversions:

- at least 5 reconstructed TPC points
- $d_0 < 5$ mm

where d_0 is the minimum distance of approach between the track and the fitted beam centroid, in the $x - y$ plane.

4 Basic principles of heavy flavour lepton tagging with Aleph

Lepton candidates arise from the following sources:

- Prompt leptons from primary b decay, $b \to \ell^- \bar{\nu}$ X.
- Prompt leptons from secondary b decays, $b \to c \to \ell^+ \nu$ X and $b \to \tau \to \ell^- \bar{\nu}$ X.
- Prompt leptons from primary c decay, $c \to \ell^+ \nu$ X.
- Non-prompt electrons from π^0 and η Dalitz decays, $\pi^0(\eta) \to e^+e^-\gamma$ and photon conversions, $\gamma \to e^+e^-$.
- Non-prompt muons from charged π and K decay, $\pi^+(K^+) \to \mu^+\nu_\mu$.
- Hadrons misidentified as leptons.

The tools to distinguish these are the lepton candidate's momentum, its transverse momentum with respect to an axis approximating the decaying hadron direction and the distance between the track and the interaction point at the point of closest approach (d_0).

In heavy flavour production at LEP the final state heavy flavour hadron almost invariably contains one of the original quarks from the Z decay, and this results in the heavy hadron having a harder momentum spectrum than the light hadrons which are formed in the hadronisation process. Simple kinematics suggests that the hardness of the spectrum will increase with the quark mass and the data support this. The momentum spectrum of the hadron is parametrised by means of a fragmentation function and for this analysis the fragmentation scheme of Peterson *et al.* [4] has been used. This has one flavour dependent parameter which determines the hardness of the spectrum. The values used [1] are $\varepsilon_b = 0.0032 \pm 0.0018$ and $\varepsilon_c = 0.066 \pm 0.014$. Using the parton shower version of JETSET, these correspond to mean energies of the b and c hadrons with respect to the beam energy of 0.714 ± 0.012 and 0.487 ± 0.011 respectively.

This hard spectrum results in energetic leptons from both primary b and c decays. This makes a lower cut on the momentum of the lepton very effective for

discrimination of the prompt signal from both misidentified hadrons and (particularly) from conversions and Dalitz electrons which have a very soft spectrum. With the ALEPH detector, muons require 3 GeV/c to traverse the iron of the hadron calorimeter and reach the muon chambers with certainty. Consequently, only leptons with momentum greater than 3 GeV/c are considered for tagging purposes. Secondary prompt leptons from b decay have a softer spectrum than primary ones but still have a harder one than the background sources.

Photon conversions into e^+e^- pairs create many electrons; typically 20 photons are produced per Z decay, of which 10% will convert in the beam pipe, the VDET, the ITC or the inner wall of the TPC. However, virtually all of these are easily eliminated by the momentum cut, the requirement that d_0 be less than 5 mm, and an algorithm which examines electron candidates for evidence that they could originate in conjunction with an opposite sign track at a point consistent with material in the detector and with a total mass of the two candidates of less than 20 MeV. Such electrons are valuable for estimation of the efficiency of the electron identification procedures.

The most important variable to discriminate primary b decays from other b and c decays is the transverse momentum, $p_\perp$. This reflects the momentum distribution in the centre of mass of the heavy hadron and is much harder for primary b decays due to the greater mass of the b hadrons. As the direction of the b hadron is not perfectly known, there is ambiguity over the reference direction which should be taken for the definition of the transverse momentum. This is crucial for the effectiveness of the separation procedures, and it is discussed in detail in section 7.

The rest frame momentum distribution for leptons from semileptonic decays of b hadrons is not perfectly known; it is the subject of a number of theoretical studies and has been measured for the upper part of the spectrum by both the CLEO and ARGUS experiments. For the Monte Carlo simulation, the model of Altarelli *et al.* [5] has been used with the parameters chosen to give agreement with the rest frame spectra from the $\Upsilon(4S)$ experiments. Other models, when fitted to the same data, yield slightly softer momentum spectra. However the differences are unimportant for the tagging investigations described in this paper.

The $p_\perp$ of the lepton will be defined with respect to the nearest jet axis, excluding the lepton itself (see section 7).

5 Electron identification

Electron identification makes use of the $\mathrm{d}E/\mathrm{d}x$ measurement in the TPC and the shape of showers in the ECAL. Basic measurements (ionization in the TPC, the pattern of energy deposition in the ECAL) are expressed in terms of normally distributed estimators on which cuts are applied to select electron candidates.

The redundancy of the TPC and ECAL information allows the performance of each estimator to be measured directly on data over a large part of the acceptance. The TPC is more effective at low electron momenta and the ECAL at higher momenta.

5.1 Electron identification in the TPC

In the TPC, the electrons liberated by a particle passing through the gas drift parallel to the beam line to the endplates of the TPC volume, where they are measured by the pulse height of the signal they cause on the endplate wires.

R_I: The parameter measuring specific ionization. For each track in the TPC, the $\mathrm{d}E/\mathrm{d}x$ is measured only when more than 50 (of a possible 330) isolated wire hits can be associated to the track. Of the measurements for the track, only the lowest 60% are taken and averaged, to avoid the large fluctuations of the Landau distribution. Each measurement is corrected for the length of the track that it has sampled. For physics analyses, a cut of 50 or more good wires is sufficient, and the efficiency of this requirement is given as a function of $p_\perp$ in figure 1 for tracks between 5 and 8 GeV/c. The efficiency is measured using all the tracks in order to obtain better statistical precision than can be obtained with the electrons alone. The lower efficiency at low $p_\perp$ is because it is more difficult to unambiguously assign a wire hit to a track (tracks are reconstructed using pad data) in the centre of a jet.

Bhabha events are used to locate the plateau of ionization for ultrarelativistic particles, whilst muons from $\mathrm{Z} \to \mu^+\mu^-$ and $\mathrm{Z} \to \tau^+\tau^-$ events are used to calibrate the relativistic rise. Tracks in hadronic events are also used to calibrate the $\mathrm{d}E/\mathrm{d}x$. These tracks are binned in momentum and each momentum bin is fitted to a sum of four contributions, for electrons, pions, kaons and protons. The pions are used for the relativistic rise, and all hadrons for the low velocity region.

All particle types are fit to a modified Bethe–Bloch formula with eight free parameters:

$$\left\langle \frac{dE}{dx} \right\rangle = \frac{P_1}{\beta^{(P_3)}} \left[P_2 + 2\log_{10}(\beta\gamma) - \beta^{P_3} - \delta \right]$$

where the density function δ is a polynomial of order 5 in $\ln(\beta\gamma)$.

The resolution of the $\mathrm{d}E/\mathrm{d}x$ values, measured with minimally ionizing pions, is 5.5% when more than 150 measurements are obtained [6].

For each track, the $\mathrm{d}E/\mathrm{d}x$ is compared to that given as the result of the above calibration with the hypothesis that the particle is an electron. The difference is expressed

$$R_I = \frac{dE/dx - \left\langle \frac{dE}{dx} \right\rangle}{\sigma_{dE/dx}}$$

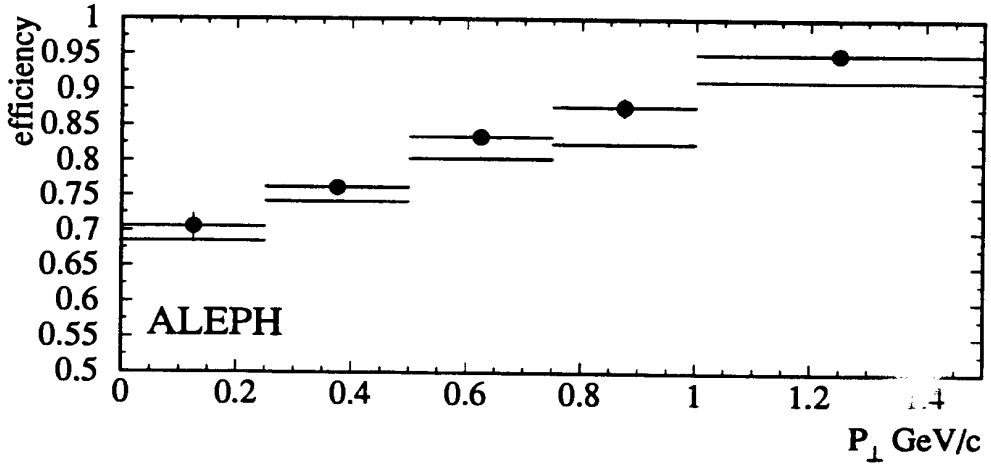

Figure 1: Fraction of tracks with 50 or more good $\mathrm{d}E/\mathrm{d}x$ measurements, for tracks between 5 and 8 GeV/c in the data. ECAL identified electrons are shown as dots, and all tracks are shown with the solid line as a function of $p_\perp$. The final bin includes all tracks with a $p_\perp$ of 1 GeV/c or more.

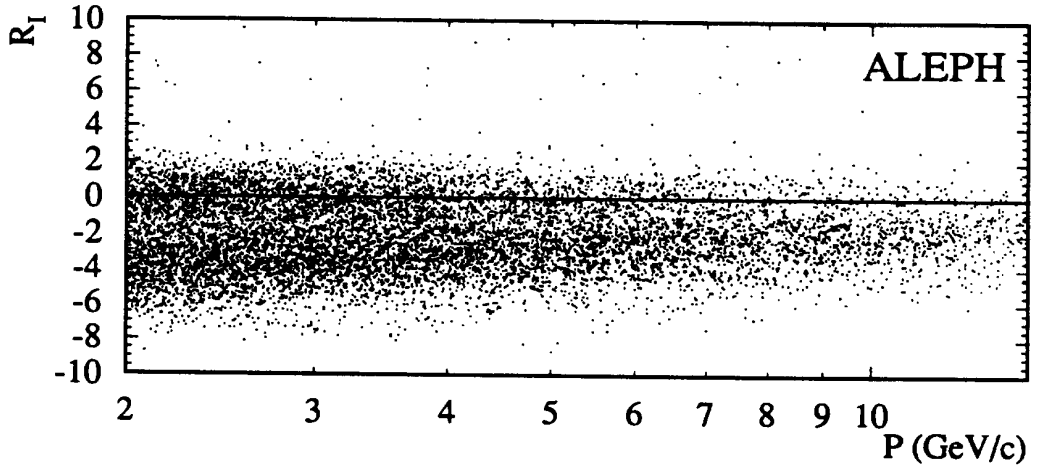

Figure 2: The number of standard deviations, R_I, from the $\mathrm{d}E/\mathrm{d}x$ electron hypothesis as a function of momentum for a sample enriched in electrons with the pair finder, as explained in section 5.3.

For a pure sample of electrons, such as is obtained from $\gamma \rightarrow e^+e^-$, R_I is very close to a gaussian of mean zero and width one. Figure 2 shows the dE/dx measurements as a function of track momentum, for a sample enriched in electrons with the pair finder as described in section 5.3. R_I is required to be greater than -2.5.

5.2 Electron identification in the ECAL

Both the compactness of the electromagnetic energy deposition around the original particle direction and the longitudinal shape of the shower are exploited.

The electromagnetic calorimeter is composed of three parts: the barrel which covers the angular domain $|cos\theta| < 0.78$, and the two endcaps which cover $0.73 < |cos\theta| < 0.97$. The small region covered by both the barrel and the endcap is called the *overlap* region. The ECAL is made of 12 *modules* in ϕ in both barrel and the endcaps. A module is formed from 45 layers of lead and proportional chambers. The readout of the chambers is made with segmented cathode *pads* connected projectively to form towers which cover approximately an angle of $0.8^o \times 0.8^o$. In each module, pads are connected in three *stacks* which give a depth segmentation corresponding to 4, 9 and 9 radiation lengths. Hence a tower has three parts: each of them is named a *storey* in the following.

The size of pads varies continuously in the barrel in order to maintain the angular size of the towers, but the situation is more complex in the endcaps. These are divided into three zones; in each zone the size of the pads varies continuously but there is a step going from one zone to the next. This introduces a geometrical effect which is taken into account for electron identification in these regions.

R_T: The parameter measuring electromagnetic shower size. Each charged track is extrapolated from the end of the TPC along a straight line and a crossing point is computed in each of the 3 stacks of the ECAL. This allows the determination in each stack of the four storeys closest to the extrapolated track. The electron estimator R_T is defined:

$$R_T = \frac{E_4/p \ - \langle E_4/p \rangle}{\sigma_{E_4/p}}$$

where:

- p is the momentum of the charged track measured in the TPC,
- $E_4 = \sum_{i,j} E_i^j \times \mathrm{Cor}(p)$; E_i^j $(i = 1,4;\ j = 1,3)$ is the energy deposited in the i^{th} selected storey of the j^{th} stack, and $\mathrm{Cor}(p)$ is a correction factor taking into account effects which are momentum dependent. For low momentum tracks, the deposited energy is corrected for zero suppression and energy lost in the inactive volumes of the ECAL, although this is negligible for energies

larger than 3 GeV. For smaller energies, the variation of the average value of E_4/p with p was studied with $\gamma\gamma \rightarrow e^+e^-$events and taken into account in the computation of R_T. The rear leakage effects are very small even at the highest energies, but are taken into account.

- $\langle E_4/p \rangle$ is the mean energy fraction deposited by an electron in the four central towers. Its value is constant with the momentum, and is equal to 0.85 in the barrel region; in the endcaps this fraction increases to 0.89 due to a geometrical focusing effect induced by the magnetic field.

- $\sigma_{E_4/p}$ is the resolution expected on the ratio; the resolution of the ECAL is worse than the resolution of the TPC up to 25 GeV, which is the range of interest for the present study.

The R_T estimator is most efficient for hadron rejection when the momentum of the track is high.

R_L: The parameter measuring electromagnetic shower depth. The shape of energy deposition induced by an electromagnetic shower is described by [7]:

$$f(t) = \frac{1}{E_0}\frac{dE}{dt} = \frac{\beta^\alpha}{\Gamma(\alpha)} t^{\alpha-1} e^{-\beta t} \qquad (1)$$

where:

- α and β are free parameters
- t is the depth in radiation length units
- E_0 is the total energy of the particle
- $\Gamma(\alpha)$ is the Euler function which normalizes $f(t)$

Electron identification relies on the study of the first moment of the longitudinal energy distribution $f(t)$:

$$< t >= \frac{\alpha}{\beta}$$

A normally distributed estimator has been built using the results of a study with electrons from test beams with energies varying from 10 to 50 GeV. It has been shown that $1/ < t >$ has a gaussian distribution [8]. This result has also been obtained and extended to lower energies with the EGS4 simulation [9]. The test beam studies have also shown that the $1/ < t >$ parameter is independent of the angle of the incoming particle.

In the data $< t >$ is computed using the energy deposited in the three stacks, with an iterative procedure which assumes at each step that the shape of the

shower is given by equation (1). This converges very quickly for electrons with energy larger than 3 GeV and rejects hadrons since in general hadronic showers do not fit the shape of an electromagnetic shower. A normally distributed estimator, R_L, is defined by:

$$R_L = \frac{(\beta/\alpha - < \beta/\alpha >)}{\sigma(\beta/\alpha)}$$

The momentum dependencies of $< \beta/\alpha >$ and $\sigma(\beta/\alpha)$ are parametrised using electrons selected in hadronic events with severe R_T and R_I cuts; electrons originating from Bhabha events are also used. The longitudinal profile information is computed on the truncated shower containing only the storeys in each stack selected to compute R_T. This is to minimize the influence of a possible overlap of two clusters produced by two different charged or neutral particles. This slightly affects the parametrisation of $< \beta/\alpha >$ with respect to the shape of a fully isolated shower.

5.2.1 Electron identification in the overlap.

The overlap of the ECAL is the region where a particle coming from the centre of the apparatus develops a shower in both the ECAL barrel and endcap. This region is 4.2% of the angular coverage of the ECAL. There are two problems specific to this region:

- Loss of energy in the dead region between the barrel and endcap, which affects the shape of the shower.
- Leakage through the rear of the calorimeter due to the smaller thickness of the ECAL in this region ($\simeq 16\ X_0$).

The analysis of the overlap region is quite complex. It has to take into account that the dead regions depend on both polar and azimuthal angle and that the losses vary with the particle momentum. The azimuthal dependence is due to cables and the TPC feet.

These are taken into account with two factors; one for leakage through the rear, which depends only on θ and ϕ. The other is for the loss in dead zones of the overlap region, which depends on both the dead material thickness and the fraction of energy found in the barrel region. These corrections have been parametrised from test beam data [10].

5.2.2 Cuts on R_T and R_L for electron identification.

Figure 3 shows the distribution of R_T versus R_L for a sample of tracks enriched in photon conversions. The electron and hadron contributions are clearly separated,

and the following cuts on R_T and R_L are optimized to maximize hadron rejection with a limited efficiency loss:

$$\begin{aligned} -1.8 &< R_L < 3.0 \\ -1.6 &< R_T \end{aligned} \tag{2}$$

No upper cut is applied on the R_T estimator because the four central towers associated to an electron can contain additional energy from a bremsstrahlung photon.

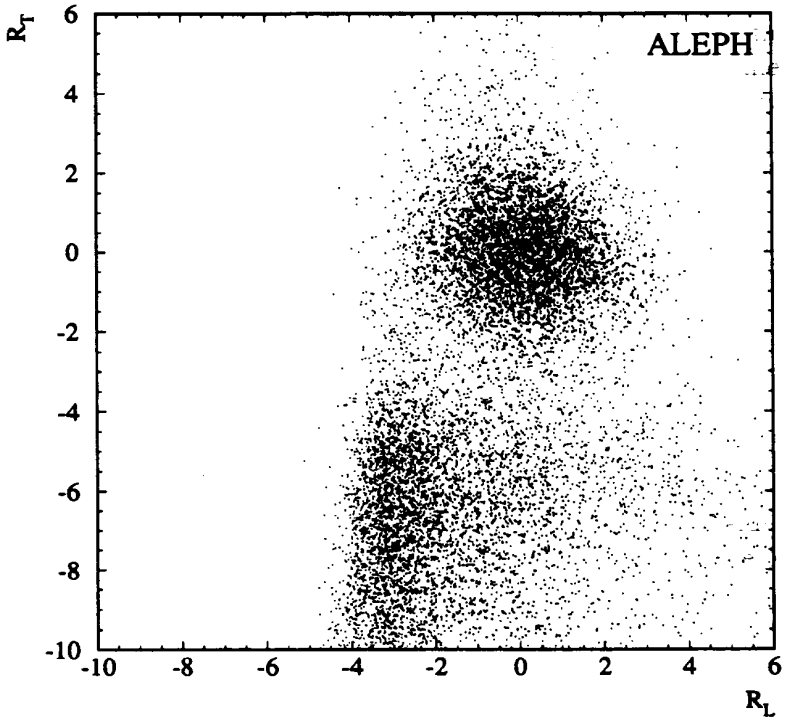

Figure 3: The estimators for electron candidates, from tracks selected with the pair finder criteria.

5.3 Measurement of electron identification efficiency

This efficiency is directly measured with data using the pairs produced by photon materialization in the beam pipe, VDET, ITC and inner wall of the TPC.

5.3.1 Identification of converted pairs

To find e^+e^- pairs from photon conversions in the detector material, each track is paired with all the tracks in the event with an opposite charge. Each possible

pair is described in terms of the distance between the reconstructed trajectories of the two particles in the $r-\theta$ and $r-\phi$ planes, computed at the point of closest approach, and in terms of the mass of the pair assuming electron masses for both particles. Both distances are required to be smaller than 1 cm, and the mass must be smaller than $20\,\mathrm{MeV/c^2}$.

With these cuts, the sample used for figure 3 still has a large hadronic contaminant. A sample with 98% purity is obtained from this sample by applying ECAL and $\mathrm{d}E/\mathrm{d}x$ electron identification cuts, and by requiring that the materialization point be in a part of the detector known to have a high density of material. Two selection criteria are used, and tracks which pass either are taken for the efficiency measurement.

- For the first criterion, ECAL and $\mathrm{d}E/\mathrm{d}x$ cuts are applied to the other track of the pair. The pair must originate from the VDET, the walls of the ITC or the inner wall of the TPC. Both tracks are required to have momenta greater than $3\,\mathrm{GeV/c}$.

- For the second criterion, the track itself must pass a hard cut on $\mathrm{d}E/\mathrm{d}x$ ($R_I >$ -0.5) and originate from the ITC outer wall or TPC inner wall.

The structure of ALEPH can be clearly seen in figure 4, which plots the radius of materialization perpendicular to the beam line.

5.3.2 Electron identification efficiency

The efficiency of the electron identification by the ECAL is measured with respect to p, $p_\perp$ and θ of the track; this is summarized in tables 1 and 2, and in figure 5. Table 2 shows no evidence for a momentum dependence, as expected from the definition of the estimators. The falloff in the efficiency in the overlap and endcap region is due to the greater number of cracks in those regions.

$\cos\theta$	0.00 - 0.73	0.73 - 0.78	0.78 - 0.90	0.90 - 0.95
$p_\perp$<0.25 GeV/c	0.825 ± 0.012	0.658±0.039	0.710±0.021	0.770±0.036
$p_\perp$>0.25 GeV/c	0.833 ± 0.009	0.753±0.027	0.721±0.017	0.724±0.033

Table 1: Efficiency of the ECAL for electron identification for $p > 3\,\mathrm{GeV/c}$. Above $p_\perp > 0.25\,\mathrm{GeV/c}$, this efficiency is independent of $p_\perp$.

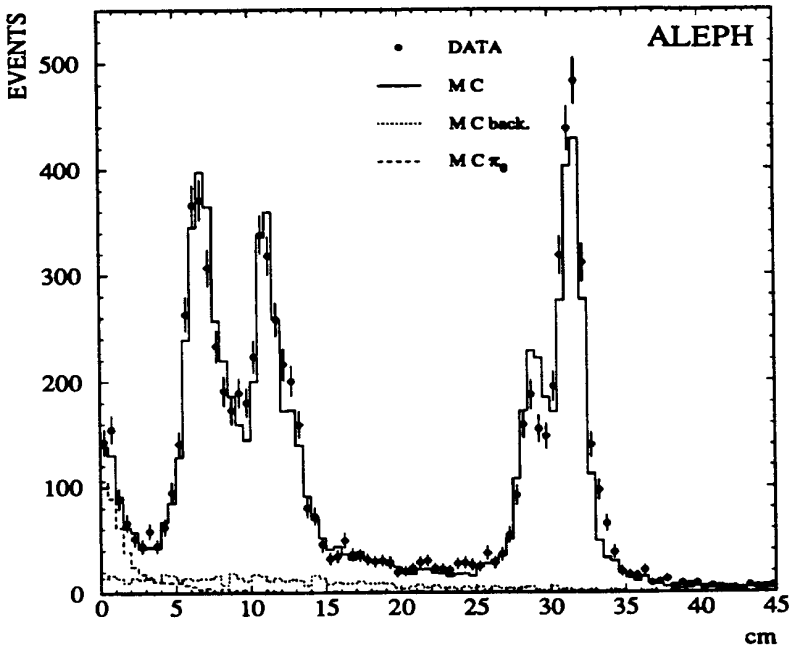

Figure 4: Materialization radius of converted pair candidates with one track satisfying the electron identification criteria as explained in the text. The five peaks correspond to: 1) Dalitz pairs, 2) Beam pipe and first layer of the VDET, 3) second layer of the Vdet and inner wall of the ITC, 4) Outer wall of the ITC and 5) Inner wall of the TPC. The continuum production between 15 and 25 cm is from wires and gas in the ITC.

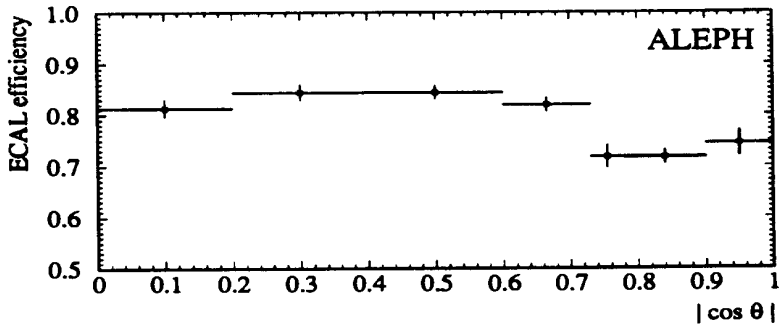

Figure 5: Efficiency of electron identification in the ECAL as a function of polar angle, as measured from photon conversions. The efficiency due to the cut $|\cos\theta| < 0.95$ is not included.

P(GeV/c)	3 - 5	5 - 8	> 8
ϵ^e	0.79 ± 0.01	0.79 ± 0.01	0.76 ± 0.02

Table 2: Efficiency of the ECAL for electron identification with respect to the electron momentum

5.4 Measurement of the contamination of the electron sample

The purity of the electron sample selected with the ECAL is measured from the dE/dx information.

Figure 6 (a, b, c) shows the R_I distribution for ECAL electron candidates in various momentum ranges. The gaussian from the electrons dominates, but the residual hadronic contamination is not negligible. The hadronic contamination is estimated by fitting the R_I distribution of the electron candidates in a (p,$p_\perp$) region to the function

$$N^e f^e(R_I) + N^h f^h(R_I)$$

Where:

- N^e and N^h are the numbers of electrons and hadrons present in the sample.
- f^e is a gaussian with free average and width which gives the shape of the electrons in the sample. The results of the fit are consistent with an average of zero and a width of one.
- f^h is the shape of the hadron R_I distribution. f_h is taken to be the distribution of tracks which are selected as hadrons in the ECAL with $R_T < -2.3$, $R_L < -2.3$.

The electron contribution is then subtracted from the data as shown in figure 6 (d, e, f) and the hadronic contamination is that part of the difference which passes the dE/dx cut of -2.5.

The above procedure is tested on Monte Carlo where the agreement between the Monte Carlo fit results and the truth values is satisfactory, as shown in figure 7. This figure shows also the misidentification probability directly extracted from data and used to compute the hadron contamination in the lepton sample. A large discrepancy in the misidentification rate is observed at low momenta between data and Monte Carlo, and hence the necessity to recalibrate the Monte Carlo from the data, as done in reference [1].

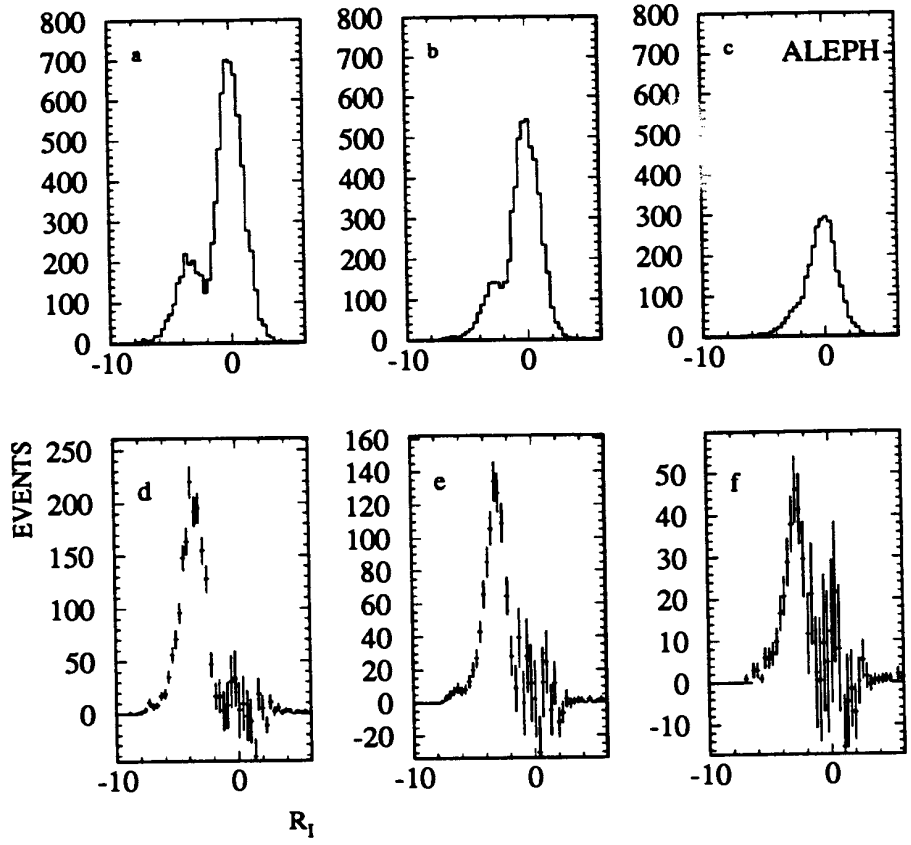

Figure 6: (a,b,c): R_I distribution for ECAL electron candidates in 3 different momentum ranges: [3,5] GeV/c, [5,8] GeV/c, and [8,11] GeV/c. (d,e,f): R_I distribution with the electron gaussian contribution subtracted.

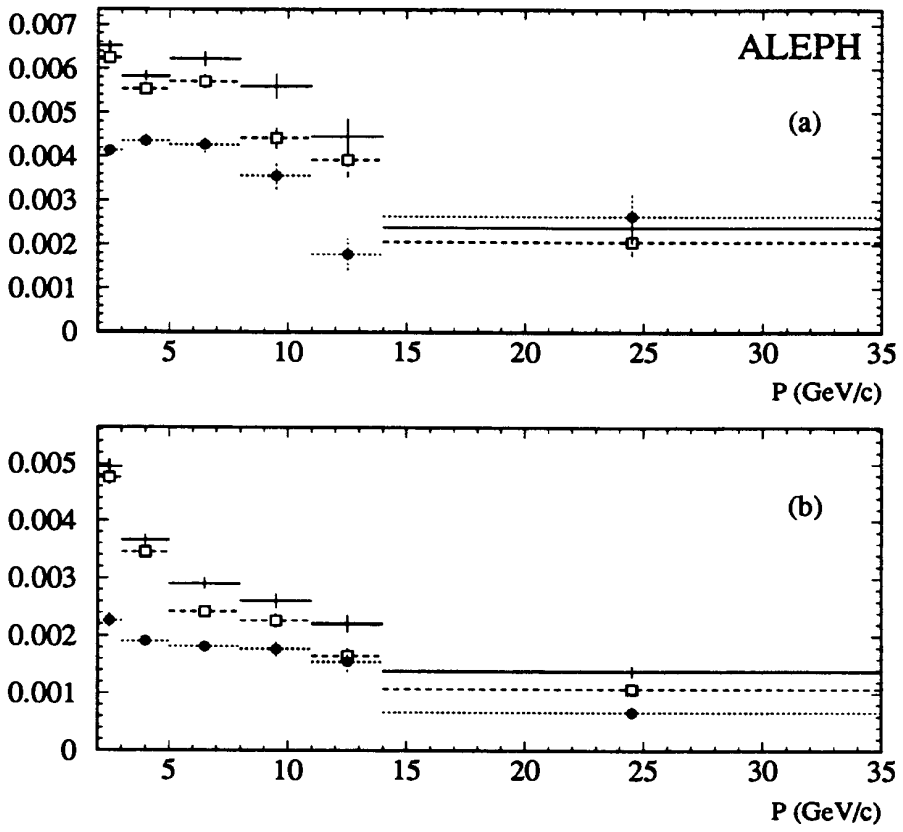

Figure 7: Probability of identifying a hadron as an electron, *vs.* momentum, before the dE/dx cut: *(a)* for $p_\perp < 0.5\,\mathrm{GeV/c}$, and *(b)* for $p_\perp > 0.5\,\mathrm{GeV/c}$. The crosses indicate the values given by the Monte Carlo, the squares give the values as a result of the fitting procedure when applied to the Monte Carlo, and the solid circles are the results of the fit when applied to the data.

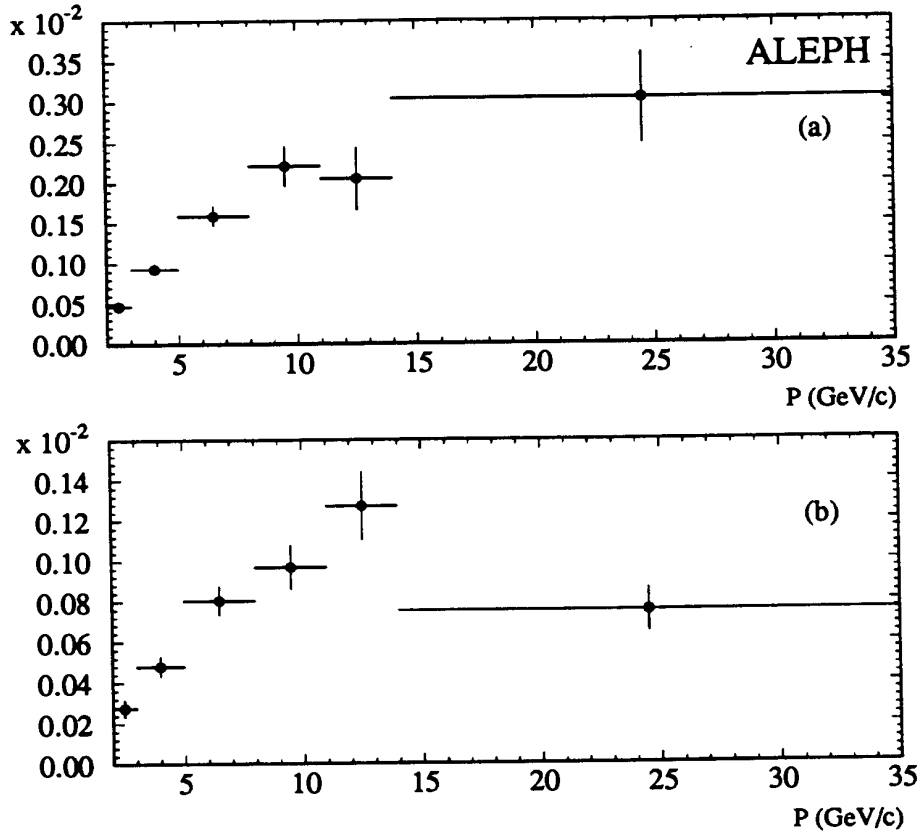

Figure 8: Probability of identifying a hadron as an electron, *vs.* momentum: *(a)* for $p_\perp < 0.5\,\mathrm{GeV/c}$, and *(b)* for $p_\perp > 0.5\,\mathrm{GeV/c}$.

5.5 Electron identification combining calorimetry and ionisation

The standard electron identification requires that both the ECAL and dE/dx criteria as defined in sections 5.1 and 5.2 are met. The simultaneous use of the two identification methods provides a misidentification probability for hadrons always smaller than 0.003 as shown in figure 8. The (p,$p_\perp$) dependence of the overall identification efficiency for electrons is given in table 3.

p(GeV/c)	3.0 - 5.0	5.0 - 8.0	> 8.0
$p_\perp$<0.25 GeV/c	0.551±0.012	0.532±0.020	0.526±0.038
0.25<$p_\perp$<0.50 GeV/c	0.609±0.019	0.536±0.028	0.531±0.031
0.50<$p_\perp$<0.75 GeV/c	0.639±0.038	0.654±0.020	0.649±0.028
$p_\perp$>0.75 GeV/c	0.767±0.012	0.731±0.027	0.700±0.028

Table 3: Efficiency of the standard electron identification

6 Muon identification

Muons are identified in ALEPH using the tracking capabilities of the Hadron Calorimeter, together with the Muon Chamber information. The Hadron Calorimeter (HCAL) consists of 23 layers of plastic limited streamer tubes separated by 5 cm thick iron slabs. The iron also serves as return yoke for the magnet and the main support for the ALEPH apparatus. Each streamer tube has an active cell size of 9×9 mm^2, a separation wall of 1 mm and is coupled capacitively on one side to pads which form towers for the measurement of the hadronic energy. On the other side, the streamer tubes are coupled to 4 mm wide aluminium strips which run parallel to the tube. The aluminium strips are used to produce a digital signal whenever the particular cell fires. Muon identification in the HCAL involves extrapolating a TPC track through the calorimeter and counting how many HCAL digital hits fall in the neighbourhood of the extrapolation. This allows the discrimination of particles which penetrate through the whole depth of the calorimeter.

Each track with momentum greater than 1.5 GeV/c is extrapolated (as if it were a muon) through the HCAL material taking into account a detailed magnetic field map and estimated energy losses. A "road" is opened around the extrapolated track, whose width is three times the standard deviation on the estimated extrapolation due to multiple scattering. An HCAL plane is said to be expected to fire if the extrapolated track intersects it within an active region; the plane is said to have fired if a digital hit lies within the multiple scattering road. For a hit to

be counted, the number of adjacent firing tubes must not be greater than three. Tracks are considered for muon identification if their momentum is greater than 3 GeV/c; this ensures that all muons exit the HCAL, independent of their crossing angle.

The HCAL plane efficiency is mapped in a detailed way in the simulation, using $Z \rightarrow \mu^+\mu^-$ events which have been selected with an algorithm which does not make use of the HCAL information.

The statistical precision which has been obtained on the plane efficiency is about 1% for the barrel and 2% for the endcaps and the average plane efficiency turns out to be about 75%. The inefficiency is due to the presence of plastic walls between tubes (13%), to geometrical dead zones within the planes (7%), and to readout inefficiencies (5%).

6.1 HCAL selection

Muons are identified with cuts consistent with a track which penetrates through the whole depth of the HCAL without showering. Such cuts are independent of momentum, since a muon above 3 GeV/c escapes the detector, and test beam data show that there are no differences in the tube firing efficiency for muons from 5 to 50 GeV/c.

The cuts used to define a penetrating track are

- $N_{fir}/N_{exp} \geq 0.4$
- $N_{exp} \geq 10$
- $N_{10} > 4$

where N_{exp}, N_{fir} and N_{10} are, respectively, the number of expected planes, the number of actually firing planes, and the number of firing planes within the last ten expected for the track. These cuts select penetrating particles and are suitable for isolated muons. To enhance the rejection power against hadron background the typical features of the digital pattern created by a hadron shower in the HCAL are used to discriminate hadrons from muons. A variable (X_{mult}) is computed by counting all the HCAL digital hits in the last eleven planes within a wide "road" (expanding from 20 cm to 30 cm) around the extrapolated track. The result is normalized by dividing by the number of firing planes so that X_{mult} represents the average hit multiplicity per firing plane and hence gives a measure on the lateral size of the digital pattern linked to the track.

The cut applied for muon identification is

$$X_{mult} \leq 1.5$$

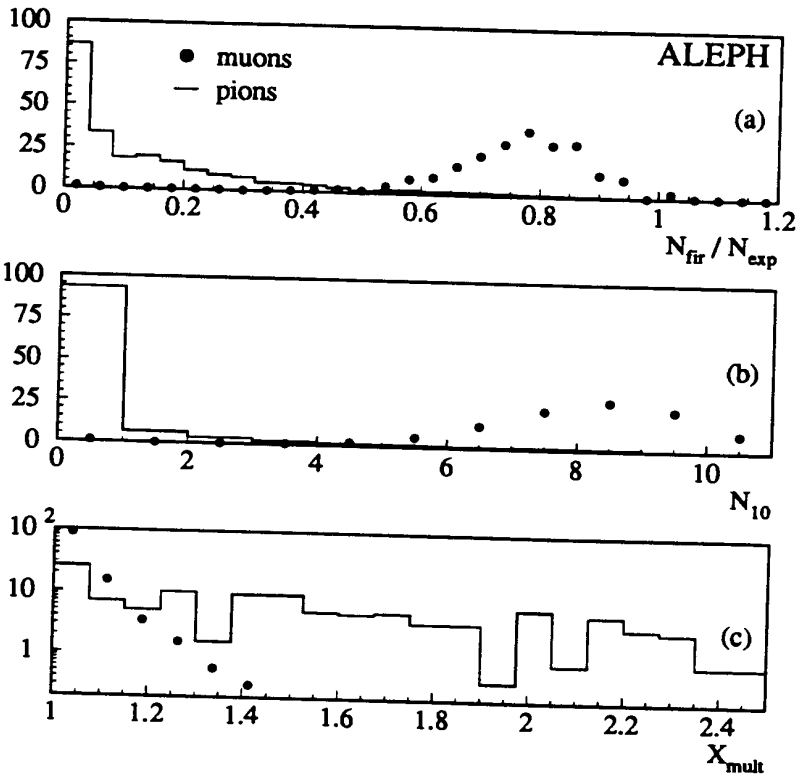

Figure 9: Distribution of N_{fit}/N_{exp} (a), N_{10} (b), and X_{mult} (c), for muons and pions, with $N_{exp} > 10$. The plots have been normalized to equal areas, and the vertical scale is arbitrary. The discontinuous nature of (a) and (c) is because these quantities are ratios of integers.

which removes about 1% of the prompt muons.

In figure 9 the distributions for N_{fir}/N_{exp}, N_{10} and X_{mult} are shown for muons coming from $Z \rightarrow \mu^+\mu^-$ events and for pions produced in the τ decay channels $\tau \rightarrow \rho\nu$, $\tau \rightarrow K^*\nu$.

6.2 Muon detector association

The Muon Detector consists of two layers of chambers separated by 50 cm, and is located behind the last iron slab of the HCAL, which is 10 cm thick. It is at 7.5 hadronic interaction lengths at normal incidence from the primary interaction point. Each layer has two planes of streamer tubes and each plane reads out orthogonal coordinates using aluminium strips. Therefore, up to two space points can be measured by each layer.

A track is defined to have hit the Muon Chambers if at least one of the two tube planes has yielded a space point whose distance from the extrapolated track is less than four times the estimated multiple scattering standard deviation.

The efficiency of the Muon Chambers has been measured with a procedure similar to that used for the HCAL, and again the results are inserted in the simulation program to account for the measured efficiencies through random hit deletion in simulation events.

The demand for the association of a Muon Chamber hit in addition to the HCAL muon criteria is very powerful for background rejection. The Monte Carlo predicts that while about 94% of the muons which have been identified in HCAL are associated to a Muon Chamber hit, only about 20% of the misidentified hadrons are associated. This is due to the two–dimensional nature of the Muon Chamber readout, compared to the one–dimensional in the HCAL, and also to the demand that the particle has passed through all the iron.

Due to the high track multiplicity inside a jet and due to the fact that the HCAL tracking is only in one projection, the multiple scattering "roads" opened around different tracks can overlap, and the same hit can be associated to more than one track. When two tracks happen to have common hits they are said to be shadowing each other and when both are identified as muons a choice has to be made. Usually the Muon Chambers with their two–dimensional points resolve the ambiguity; when both tracks share exactly the same Muon Chamber hits, the one with the minimum hit–to–track distance is chosen. The fraction of prompt muons lost because of inefficiencies in the shadowing algorithm is 0.4 % at $p_\perp < 1.25\ GeV/c$ and less than 0.1 % at $p_\perp > 1.25\ GeV/c$.

Penetrating tracks (as defined in section 6.1) which are associated to at least one plane of the Muon Chambers and which are the best muon candidate when there is a shadowing ambiguity are defined as muons.

6.3 Muon identification efficiency

The muon identification efficiency, computed from real isolated muons, is given as a function of the cosine of the polar angle in figure 10. The two dips in the efficiency are due to the ALEPH iron supports which are not instrumented with muon chambers.

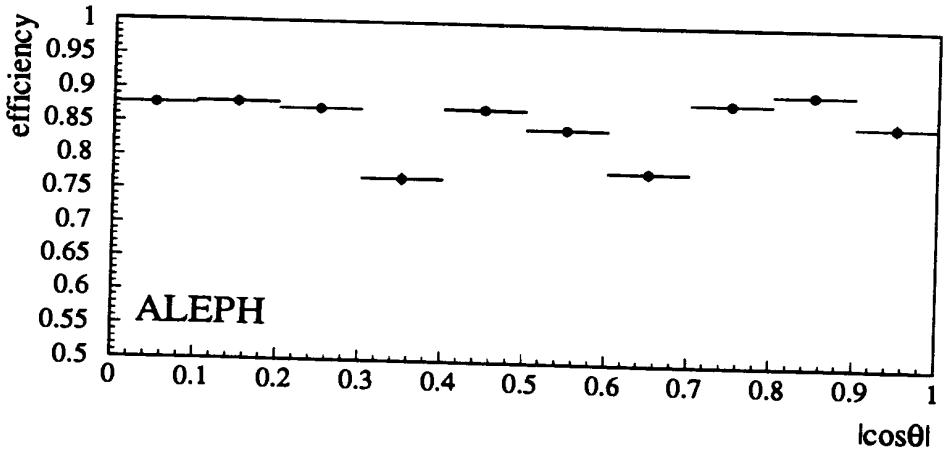

Figure 10: Efficiencies of the muon selection as a function of $\cos\theta$ for isolated muons. The efficiency due to the cut $|\cos\theta| < 0.95$ is not included.

The momentum independence of the muon identification efficiency has been verified by selecting muons produced in τ decays. The selection is based on single prong τ decays (not accompanied by neutrals) which behave as minimally ionizing particles in the ECAL, and have less than 8 GeV of energy deposited in the HCAL towers. With this sample the Muon Chambers can be used to check the HCAL identification criteria and vice versa. Figure 11 shows the effect of the additional requirement of at least one muon chamber hit and the effect of the four cuts on N_{fir}/N_{exp}, N_{exp}, N_{10} and X_{mult}, as seen in the selection of muons from taus. The efficiencies of these cuts are constant throughout the whole momentum range of 3 to 40 GeV/c, and the agreement between data and Monte Carlo is good.

The jet environment can modify the efficiency of muon identification in two ways. As was discussed above, a fraction of muons is lost because the identification is assigned to a nearby track (shadowing). This fraction, as calculated with the Monte Carlo, is very small (0.4% at low $p_\perp$) and the resulting uncertainty in the identification efficiency is negligible.

Another way nearby hadrons can affect the efficiency is by modifying the value of N_{fir}/N_{exp}, N_{10}, X_{mult}. This has been studied by comparing clean samples of

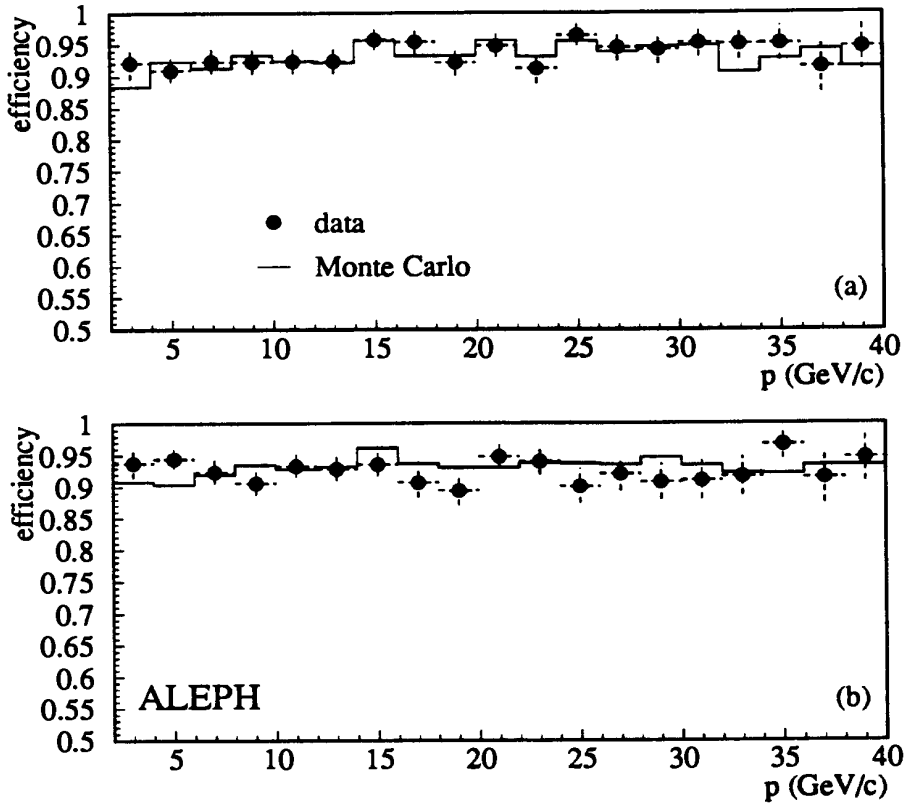

Figure 11: (a): Efficiency of the Muon Chambers identification criteria *vs.* momentum for the τ sample. The HCAL is used to select the candidates. (b): Efficiency of the HCAL identification criteria *vs.* momentum for the τ sample. The Muon Chambers are used to select the candidates.

	$p_\perp$<1.25	$p_\perp$>1.25
3 <p< 5	83.8 ± 1.0	83.3 ± 0.8
5 <p< 10	85.3 ± 1.0	84.5 ± 0.6
p> 10	86.3 ± 1.6	86.6 ± 0.6
total	84.8 ± 0.7	85.0 ± 0.4

Table 4: Muon identification efficiency (%) versus p and $p_\perp$ (GeV/c) in the Monte Carlo after mapping corrections from dimuon events. The uncertainty is statistical only.

muons in data and Monte Carlo selected with tighter cuts on the muon chambers. The resulting uncertainty on the identification efficiency turns out to be less than 2%. Table 4 gives the efficiency for muon identification versus p and $p_\perp$ obtained after applying the mapping corrections to the Monte Carlo $q\bar{q}$ events.

6.4 Hadron misidentification

In hadronic Z decays prompt muons are approximately 0.5% of the charged tracks, and so the muon identification algorithm has been tuned not only to identify muons with high efficiency, but also to give a very good hadron rejection power. A hadron can fake a muon by decaying to a muon before entering the HCAL, and is, as far as the Hadron Calorimeter and the Muon Chambers are concerned, indistinguishable from a prompt muon. Hadrons can fake muons also by not interacting in ALEPH (sail-through) or by interacting in such a way that they are recognized as a muon by the algorithm (punch-through).

As far as the decays are concerned, it is convenient to separate those which occur within the TPC volume from the ones which take place in the calorimeters. Since the pion and kaon lifetimes and decay modes are well established, the first class is affected only by the uncertainty in the ratio between pion and kaon production rates and the simulation of the effect of kinks on the tracking. The systematic uncertainty on this kind of background is assumed to be less than 10%. When hadrons enter the calorimeters, the decay rate depends also on the interaction cross section with the material. This background is therefore treated together with sail-through and punch-through and is referred to as *non-decaying hadrons.*

The capability of the Monte Carlo to simulate the various backgrounds has been checked with pure samples of hadrons selected from τ decays (using the channels $\tau \to \rho\nu$, $\tau \to K^*\nu$, $\tau \to \pi\pi\pi\nu$) and K^0 decays ($K^0 \to \pi\pi$). For the non-decaying hadrons, which proves to be the most difficult background to correctly simulate, the ratio of misidentification probability in data to Monte Carlo has

	$p_\perp$<1.25	$p_\perp$>1.25
3 <p< 5	0.43 ± 0.03	0.44 ± 0.03
5 <p< 10	0.42 ± 0.03	0.43 ± 0.03
p> 10	0.33 ± 0.07	0.36 ± 0.05
total	0.41 ± 0.02	0.42 ± 0.02

Table 5: Hadron misidentification probability (%) for punch-through and sail-through versus p and $p_\perp$ (GeV/c) in the corrected Monte Carlo. The uncertainty is statistical only.

	$p_\perp$<1.25	$p_\perp$>1.25
3 <p< 5	0.48 ± 0.03	0.54 ± 0.03
5 <p< 10	0.39 ± 0.03	0.41 ± 0.03
p> 10	0.25 ± 0.06	0.23 ± 0.05
total	0.43 ± 0.02	0.45 ± 0.02

Table 6: Hadron misidentification probability (%) due to pion or kaon decay versus p and $p_\perp$ (GeV/c) in the corrected Monte Carlo. The uncertainty is statistical only.

been measured to be:

$$R_{mis} = 1.16 \pm 0.21 \pm 0.09$$

where the first uncertainty is statistical and the second comes from the uncertainty in the sample composition and the uncertainty due to the decays simulation. The hadron rejection power of the muon identification algorithm is given (versus p and $p_\perp$) in tables 5 and 6 for Monte Carlo $q\bar{q}$ events, after the above corrections.

7 Jet clustering and $p_\perp$ definition

The definition of the transverse momentum of the lepton has been optimized in order to obtain the best separation between primary semileptonic b decays and other processes. Since the transverse momentum is defined with respect to the axis of the jet, a proper tuning of the jet clustering algorithm is mandatory. The most effective definition requires the use of neutrals as well as charged tracks for the jet definition and that the lepton be removed from the jet before the axis is defined.

7.1 Jet definition from neutral and charged energy

For the jets, an energy flow algorithm as outlined in reference [11], is used in which the measured charged particle momenta and the energy deposits in both calorimeters are used. Use of the charged particle momenta yields a better energy flow resolution than the calorimeters alone, and so calorimeter clusters associated to charged tracks are not counted. Jets are formed using:

- tracks which pass the criteria used in the event selection
- long lived neutral particles which decay into a pair of oppositely charged particles (V^0)
- photons which are identified by virtue of their shower profile in the ECAL
- energy deposits in the electromagnetic and hadron calorimeters which are classified as being produced by neutral hadrons; this is made on the basis of the shower profile and the track–calorimetric cluster association.

In figure 12 the peak of the reconstructed energy in $q\bar{q}$ events is shown, together with the detail of the contributions: charged tracks, photons and neutral hadrons.

The clustering algorithm used is the JADE Scaled Minimum Invariant Mass algorithm [12]. The value of M_{jet} is fixed, independently of the centre–of–mass energy, to a value of $6\,\mathrm{GeV/c^2}$, which corresponds to a value of y_{cut} near 0.0044 at the peak energy. The choice has been made to optimize the purity *vs.* efficiency curve.

This algorithm does not explicitly forbid jets that are made entirely or mostly out of a single particle, which can happen because some of the particles in the event may be outside the fiducial limits. It also can happen because jets of low multiplicity do occur, albeit at a low rate. Those cases where the lepton has a momentum over 0.9 times the energy of the jet or where the jet has been formed out of less than three particles are removed from the analyses. Each event is required to have two or more jets. Overall, this introduces a bias towards $b\bar{b}$ events which is about 0.6%. The use of the energy deposits in the calorimeters for the jet definition is crucial to increase the purity of the sample. When only charged tracks are used, longer tails in the $c \to \ell^+$ and $b \to c \to \ell^+$ $p_\perp$ spectra lead to a lower $b \to \ell^-$ purity, particularly for hard cuts.

The trend of the sample composition *vs.* the $p_\perp$ cut is shown in figure 13. When only charged tracks are used, a value of y_{cut}= 0.02 is used, the one which maximizes the purity in that case. The 'lepton excluded' definition of $p_\perp$ (see section 7.2) is used here.

In some analyses the direction of the initial b quark has to be estimated. This is usually done with the direction of the thrust axis, signed with the charge of the lepton or with a jet–charge technique. In figure 14 it is shown that the direction

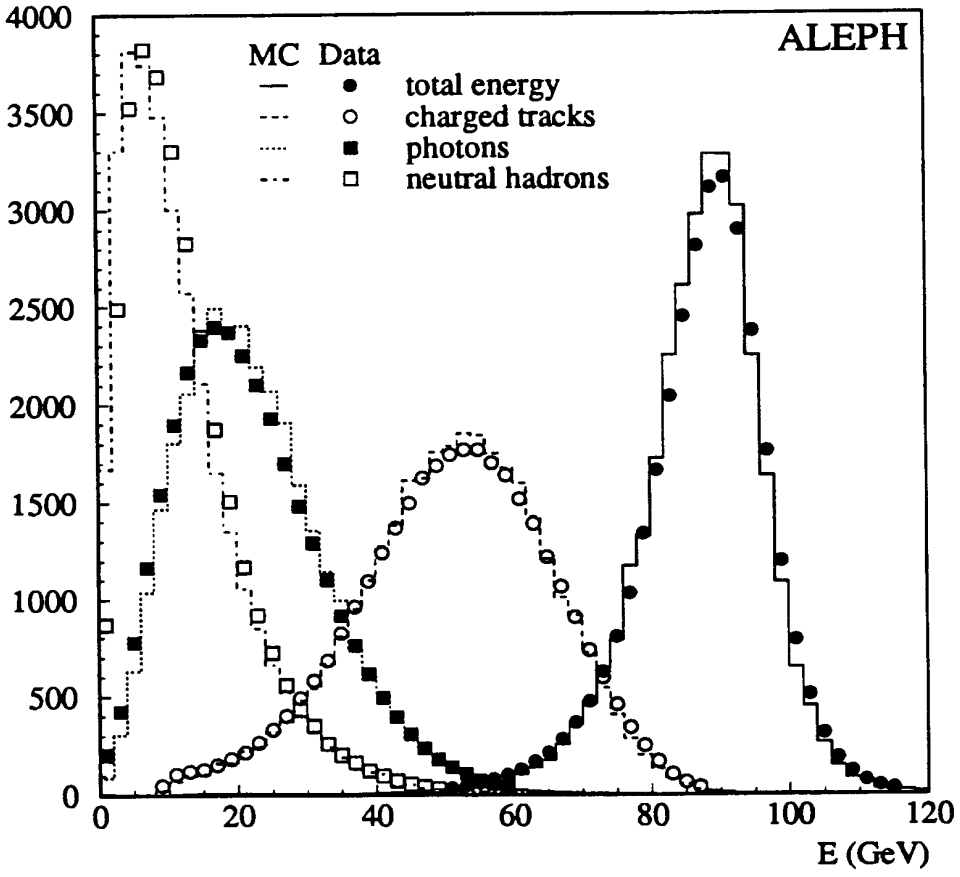

Figure 12: The energy flow peak in the Monte Carlo, with the detail of the contributions.

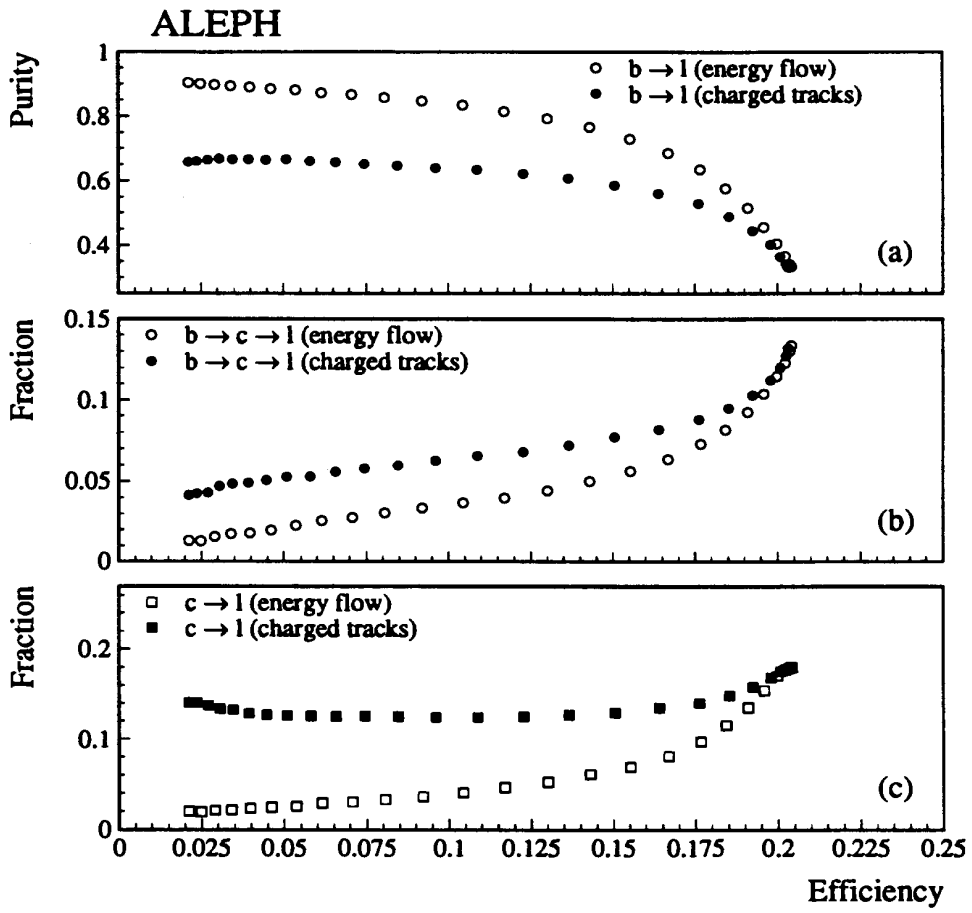

Figure 13: Comparison between the use of charged tracks alone and the inclusion of neutrals in the jet definition, as a function of $p_\perp$ cut. (a): $b \to \ell^-$ purity *vs.* $b \to \ell^-$ efficiency in the single lepton sample, from the Monte Carlo. (b) and (c): contamination rates *vs.* $b \to \ell^-$ efficiency. The $p_\perp$ cut is 0 GeV/c for the last point on the right hand side.

of the initial b quark is much better described by the thrust axis direction if also neutrals are included in the thrust computation.

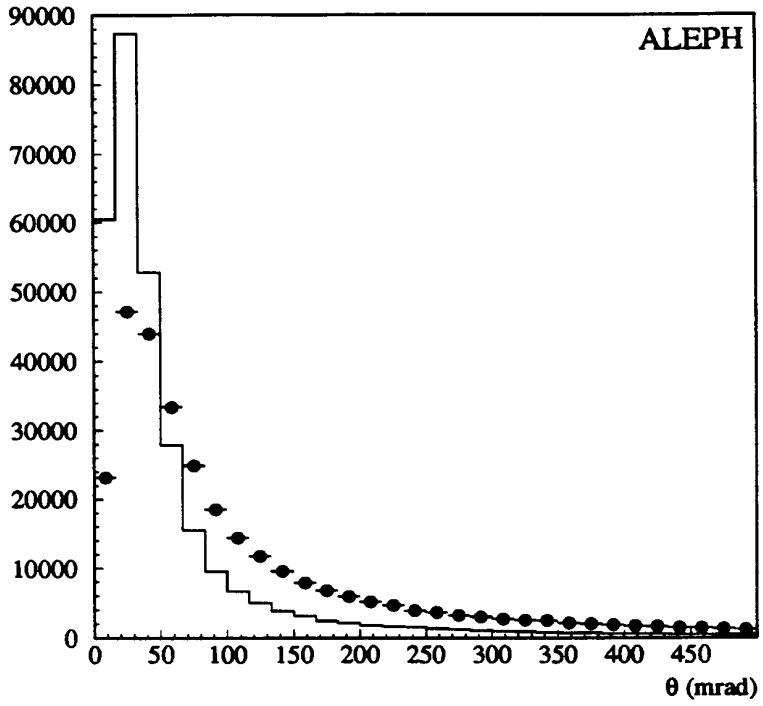

Figure 14: Angle between the initial b quark direction and the thrust axis in $b\bar{b}$ events, defined including neutrals (solid line), and using only charged tracks (solid circles).

7.2 Lepton included or excluded in the jet axis definition

When defining the $p_\perp$ of the lepton with respect to jet axis the question arises whether or not the lepton is to be included in the computation of the jet direction. The two $p_\perp$ definitions can be written as follows:

$$p_\perp^{incl} \equiv \frac{\left|\vec{p}_\ell \times \vec{p}_{jet}\right|}{\left|\vec{p}_{jet}\right|}$$

$$p_\perp^{excl} \equiv \frac{\left|\vec{p}_\ell \times (\vec{p}_{jet} - \vec{p}_\ell)\right|}{\left|\vec{p}_{jet} - \vec{p}_\ell\right|}$$

The transverse momentum is used to separate different physical components. The main advantage of the $p_\perp^{excl}$ definition is that it allows a better separation of $b \to c \to \ell^+$ from $b \to \ell^-$. The $b \to \ell^-$ efficiency *vs.* purity for both $p_\perp$ definitions, as a function of the applied $p_\perp$ cut is shown in figure 15. The efficiency is defined as the number of detected $b \to \ell^-$ decays divided by the total number of $Z \to b\bar{b}$ decays. The efficiency of the $p > 3\,\mathrm{GeV/c}$ cut is about 75% and is included in this figure. As can be seen, the resulting signal ($b \to \ell^-$) purity is higher with the $p_\perp^{excl}$ definition.

For the physics analyses which use a double lepton tag, the gain in using the $p_\perp^{excl}$ definition is even greater, since requiring one lepton in each hemisphere with high $p_\perp$ automatically reduces the charm background. This is shown in figure 16, where the efficiency is defined as the number of detected $(b \to \ell^-)(\bar{b} \to \ell^+)$ decays divided by the total number of $Z \to b\bar{b}$ decays.

8 Conclusions

The ALEPH detector has been shown to have excellent performance for the identification of inclusive leptons in hadronic Z decays.

Above 3 GeV/c inclusive prompt electrons are detected by means of the shower profile in the electromagnetic calorimeter and the ionization loss measurements in the TPC with an efficiency varying with momentum and transverse momentum from 50 to 75%, but with a very low hadron misidentification probability of typically 0.1%. Using the hadron calorimeter and the muon chambers, muons are identified with an efficiency close to 90% and a hadron misidentification probability of less than 1%.

Separation of the sources of prompt leptons from heavy quark decays is critically dependent upon the estimation of the transverse momentum of the lepton with respect to the direction of the parent hadron. It has been shown that it is highly beneficial to use both neutrals and charged tracks for the jet analysis which isolates heavy quark jets and then to exclude the lepton from the jet for the determination of the axis. The axis obtained in this way gives the transverse momentum definition which is most effective in distinguishing leptons from the primary b decays from those from other sources.

9 Acknowledgments

We thank our colleagues in the accelerator divisions for the continued good performance of LEP. Thanks also to the many engineering and technical personnel at CERN and at the home institutes for their contributions to the performance of the ALEPH detector. Those of us from non-member states thank CERN for its hospitality.

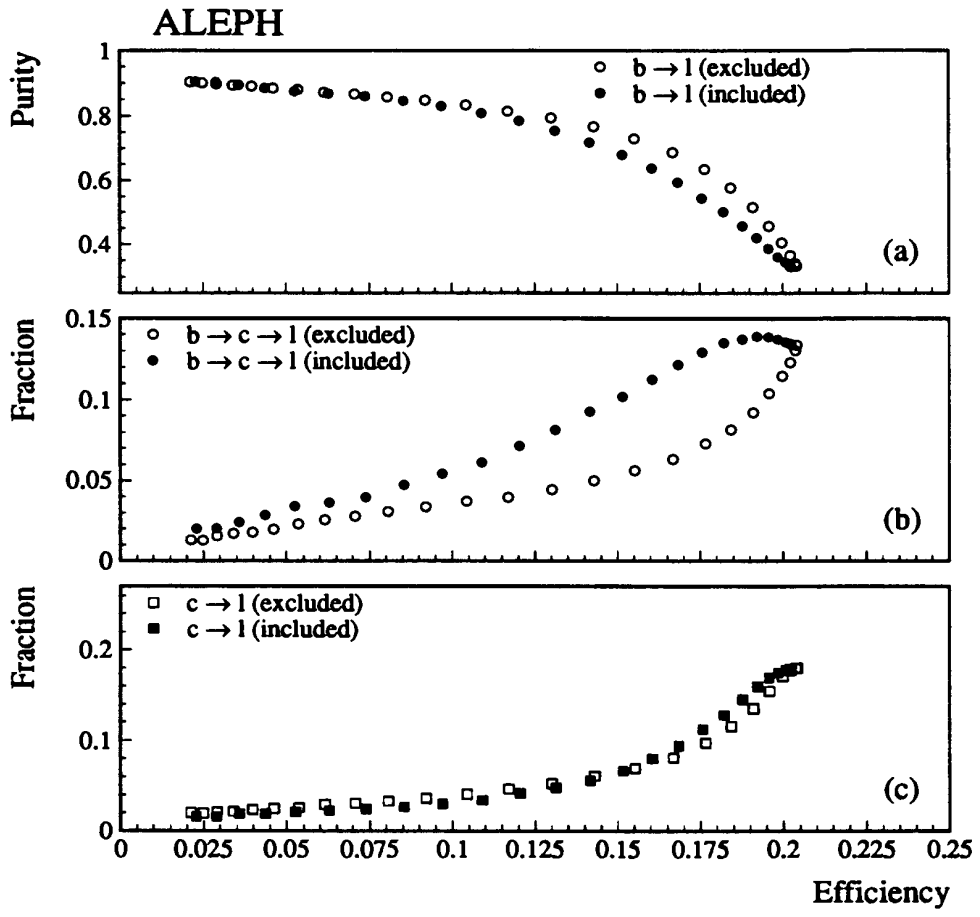

Figure 15: Comparison between the effect of the $p_\perp^{incl}$ and the $p_\perp^{excl}$ definition for various $p_\perp$ cuts. (a): $b \to \ell^-$ purity *vs.* $b \to \ell^-$ efficiency in the single lepton sample, from the Monte Carlo. (b) and (c): contamination rates *vs.* $b \to \ell^-$ efficiency. The $p_\perp$ cut is 0 GeV/c for the last point on the right hand side.

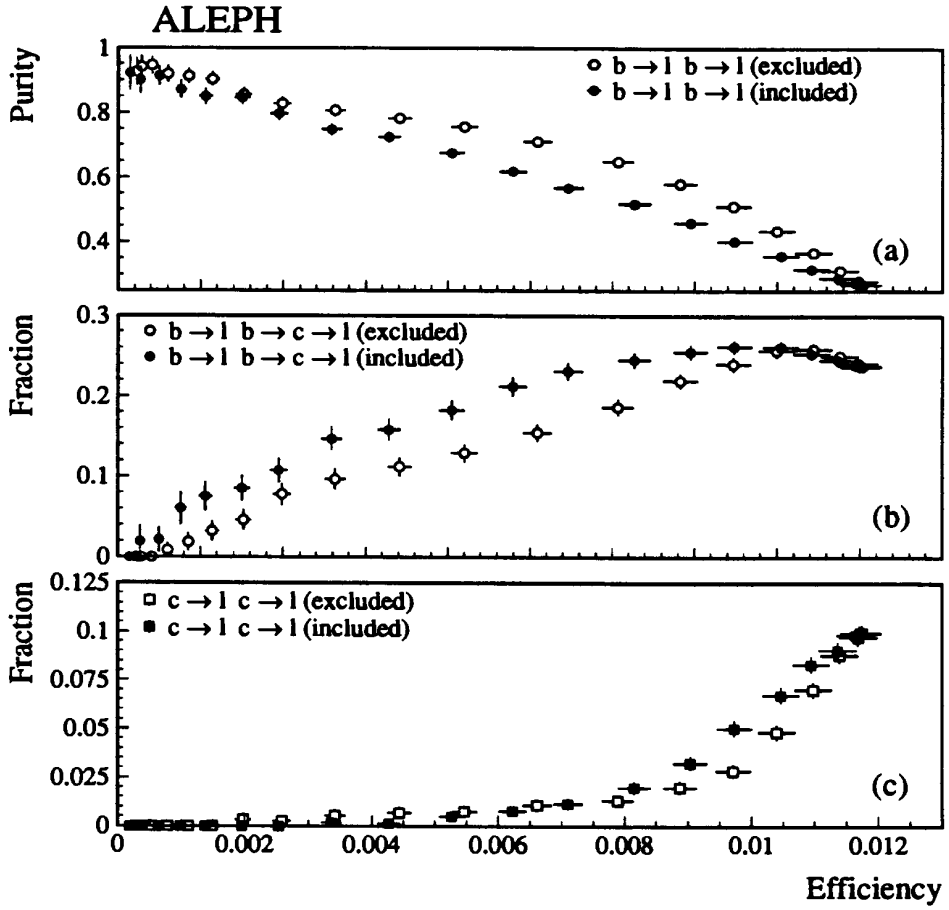

Figure 16: Comparison between $p_\perp^{incl}$ and $p_\perp^{excl}$ definition for various $p_\perp$ cuts. (a): $(b \to \ell^-)(b \to \ell^-)$ purity *vs.* $(b \to \ell^-)(b \to \ell^-)$ efficiency in the dilepton sample, from the Monte Carlo. (b): contamination rates *vs.* $(b \to \ell^-)(b \to \ell^-)$ efficiency. The $p_\perp$ cut is 0 GeV/c for the last point on the right hand side.

References

[1] ALEPH Coll., D. Decamp *et al.* , *Heavy Flavour Production and Decay with Prompt Leptons in the ALEPH Detector*, to be published, Z. Phys.

[2] ALEPH Coll., D. Decamp *et al.* , Nucl. Instr. Methods. **A294** (1990) 121
ibid., **A303** (1991) 393

[3] ALEPH Coll., D. Buskulic *et al.* , Z. Phys. **C60** (1993) 71

[4] C. Peterson *et al.* , Phys. Rev. D **27** (1983) 105

[5] G. Altarelli *et al.* , Nucl. Phys. B208 (1982) 365
G. Altarelli and S. Petrarca, Phys. Lett. B261 (1991) 303

[6] W.B. Atwood, *et al.* , Nucl. Instr. Methods. **A306** (1991) 446

[7] E. Longo and I. Sestili, Nucl. Instr. Methods. **128** (1987) 283

[8] Y. Saadi - PhD Thesis — Université de Clermont, 1989 PCCF T/89-06 Sept. 1989

[9] W.R. Nelson, H. Hirayama, and D.W.O. Rogers, "The EGS4 Code System", SLAC-265, (1985)

[10] P. Marotte — PhD Thesis — LAL Orsay, 1989 LAL 89-17 May 1989

[11] ALEPH Coll., D. Decamp *et al.* , Phys. Reports **216** (1992) 253

[12] JADE Coll., S. Bethke *et al.* , Phys. Lett. **B213** (1988) 235